Monolayer alkali and transition-metal monoxides: MgO, CaO, MnO, and NiO

F. Shayeganfar,[1,2] K. S. Vasu,[3] R. R. Nair,[3] F. M. Peeters,[4] and M. Neek-Amal[1,*]
[1]*Department of Physics, Shahid Rajaee Teacher Training University, 16875-163 Lavizan, Tehran, Iran*
[2]*Department of Civil and Environmental Engineering, Rice University, Houston, Texas 77005, USA*
[3]*School of Physics and Astronomy, University of Manchester, Manchester M13 9PL, United Kingdom*
[4]*Department of Physics, University of Antwerp, Groenenborgerlaan 171, B-2020 Antwerpen, Belgium*
(Received 6 August 2016; revised manuscript received 10 January 2017; published 19 April 2017)

Two-dimensional crystals with strong interactions between layers has attracted increasing attention in recent years in a variety of fields. In particular, the growth of a single layer of oxide materials (e.g., MgO, CaO, NiO, and MnO) over metallic substrates were found to display different physical properties than their bulk. In this study, we report on the physical properties of a single layer of metallic oxide materials and compare their properties with their bulk and other two-dimensional (2D) crystals. We found that the planar structure of metallic monoxides are unstable whereas the buckled structures are thermodynamically stable. Also, the 2D-MnO and NiO exhibit different magnetic (ferromagnetic) and optical properties than their bulk, whereas band-gap energy and linear stiffness are found to be decreasing from NiO to MgO. Our findings provide insight into oxide thin-film technology applications.

DOI: 10.1103/PhysRevB.95.144109

I. INTRODUCTION

The successful isolation of graphene [1] has motivated the exfoliation of other layered materials such as, e.g., MoS_2, h-BN, and phosphorene [2,3] and the study of the electronic, optical, and mechanical properties of their mono- and few-layer two-dimensional (2D) crystals. However, preparing monolayer metal oxide materials is still a challenge, while they may have great potential applications in physics, chemistry, and material science. In fact, metal atoms prefer to form three-dimensional (3D) close-packed structures in contrast to graphitelike layered structures which have strong in-plane interaction and weak van der Waals interaction between layers [2]. There are a few studies aimed at the synthesis of ultrathin metallic materials. For instance, Duan *et al.* [4] reported fabrication of poly-supported single-layered rhodium nanosheets using a facile solvothermal method, and Yin *et al.* [5] studied the synthesis, formation mechanism, and mechanical property of multilayered ultrathin palladium nanosheets.

More recently, synthesis of various single-layer to few layers of monoxide nanocrystals (MgO, CaO, CuO) were shown possible by trapping an aqueous solution of corresponding salt in graphene nanoenclosures [6]. Due to the light confinement and existence of large (1 GPa) van der Waals pressure in these nanoenclosures, trapped salt solutions were reached with water at room temperature, leading to 2D crystals of corresponding oxides. These findings led us to propose the structure and electronic properties of monolayers of metal oxides.

Monalyer monoxides (MMOs) with two different types of elements and cubic structure can form thin oxide films [7]. These metal-oxide surfaces can exhibit catalytic properties useful for the fabrication of gas sensors and electronic and photonic devices [7–10]. They also can be used in ceramics. The physical properties of metal-oxide thin films can be different from their bulk. Thin films of MgO (one to five layers) deposited over Ag can cause crumpling in the first layer due to the small lattice mismatch between the substrate and the MgO cubic structure [8,11]. The preparation of high-quality crystalline calcium-oxide (CaO) films is more difficult as compared to that of MgO. The CaO thin films have been grown on a Mo(001) support [12] and exhibited similar electronic and optical properties of bulk CaO.

On the other hand, antiferromagnetic (AFM) transition-metal monoxides, which can be grown as high-quality thin films on appropriate substrates, have relatively high AFM ordering temperature (Néel temperature) [13,14]. Their magnetic properties can be described by the Ising formalism and their insulating nature is due to the strong atomic electronic correlations. Anderson's superexchange theory explains the interplay between charge and magnetic ordering [15]. Thin films of metallic monoxide containing 3*d* transition metals sucha as Mn, Fe, Co, or Ni have important applications in magnetic device technology (see Ref. [16] for a review on this topic). There is growing interest in the research on metal oxides because of their fundamental electronic properties and their potential applications in different areas such as spintronics and spin valves based on the giant magnetoresistance [17–19].

Manganese oxide (MnO) is an excellent and old model system used to investigate many kinds of magnetic effects at the surface of an AFM. Epitaxial growth of MnO films has been reported on Ag(001) substrate and Pd(100) single-crystal surface [20,21]. Nickel oxide (NiO) thin films (*p*-type oxide semiconductor) can also be deposited on a glass substrate using an inexpensive spray pyrolysis technique [16,22,23]. Moreover, the NiO-layer insertion between the active organic layer showed cell power conversion efficiencies as high as 5.2% [10]. Recently, Ho *et al.* [24] reported a main excitonic emission of 3.25 eV at 300 K and donor-acceptor-pair irradiations at lowered temperatures down to 10 K. NiO thin-film nanotower was found to be an applicable material appropriate for UV luminescence and transparent-conducting-oxide applications [24].

Despite a large number of studies on thin films of MMOs, the electronic, structural, and optical properties of monolayer

*mehdi.neekamal@gmail.com

TABLE I. Comparison of the physical properties of the buckled monolayer-$XO(100)$ (X = Mg, Ca, Mn, and Ni) with those for graphene, h-BN, and MoS_2, i.e., lattice constant (a), bond distance X-O (d), the buckling height (δ), electronic band-gap energy (Δ), magnetic moment (μ_B), the in-plane stiffness (Y), and total energy per atom (E_T). The numbers inside brackets are the experimental results for bulk MMOs. In the LDA+U and GGA+U, results for U_{eff} are presented (see Sec. II).

2D crystal	a (Å)	d (Å)	δ (Å)	E_T (eV)	Δ (eV)	M (μ_B)	Y (J/m^2)
Graphene (LDA)	2.46	1.42	0	−81.13	0	0	335
h-BN (LDA)	2.49	1.45	0	−96.65	5.5 (5–7 [70])	0	300
MoS_2 (LDA)	3.18	2.34	±1.6	−140.4	1.76 (1.23 [71])	0	378 (343 [72])
MgO (LDA)	3.9	1.95	±0.3	−268.69	3.82 (6.1)	0	118 (248 [73])
(PBE+D)	4.03	2.01	±0.3	−283.31	4.04		
CaO (LDA)	4.6	2.3	±0.4	−285.1	2.03 (4.66)	0	346 (224 [13])
(PBE+D)	4.72	2.36	±0.4	−298.77	2.8		
MnO (LDA+U)	4	2	±0.5	−429.67	0.88 (3.6)	5 (0)	470 (245 [13])
(GGA+U)	4.14	2.07	±0.5	−443.65	1.18		
NiO (LDA+U)	3.84	1.92	±0.25	−712.77	1.21 (3.8)	2 (0)	687 (388 [13])
(GGA+U)	3.95	1.97	±0.25	−728.69	1.45		

nonmagnetic or ferromagnetic MMOs have not been explored. In this paper, we systematically study the electromechanical and optical properties of square lattice monolayer (which was experimentally observed by encapsulated bilayer graphene [6]) of MgO and CaO as two nonmagneticmonoxides and NiO and MnO as two AFM transition-metal monoxides. We found that a planar structure of MMO layer is unstable, while the buckled structure is stable. Monolayers of MnO and NiO have a net magnetic moment with smaller electronic band gap as compared to monolayers of MgO and CaO. The in-plane stiffness of NiO (MgO) is found to be largest (smallest) among the here investigated monolayers.

II. METHODS

Self-consistent density functional theory (DFT) calculations were used to study the electronic properties of MMOs employing the SIESTA software package [25]. We used pseudopotentials that reproduce all-electron eigenvalues and excitation energies of multiple atomic configurations. The calculations were performed within the localized spin-density approximation (LDA) and Perdew-Burke-Ernzerhof exchange-correlation functional with dispersion (PBE+D) for magnesium and calcium, and the LDA(GGA)+U (Hubbard-corrected DFT energy functionals) for nickel and manganese, in conjunction with a double-ζ polarized orbital for the basis sets and a norm-conserving Troullier-Martins-type pseudopotential for magnesium, calcium, nickel, and manganese atoms. In this work, we considered $U_{eff} = U - J$ and therefore, the electronic properties of monolayers depend on the difference of both parameters. To calculate an accurate electronic band structure, the sampling of the Brillouin zone (BZ) includes a fine $18 \times 18 \times 1$ Monkhorst-Pack k-point grid for all structures studied. A similar fine grid was used to produce an accurate band structure. The geometry optimization was pursued until the convergence criterion was less than 10^{-5} eV for total energy and less than 0.01 eV/Å for forces. The vibrational frequencies of MMOs are determined in the linear response framework. Dynamical matrices are computed at eight wave ($\vec{q}$) vectors in the irreducible wedge of BZ, i.e., on an $8 \times 8 \times 8$ grid [26].

Concerning the underestimation of the total energy and the energy gap by the LDA approach and the weakness of LDA in describing dispersion forces, we compare the total energy and other characteristics presented in Table I by considering the PBE+D correction functional.

Optical properties of MMOs were computed using the BERKELEYGW package based on first-principles many-body perturbation theory [27] (see more details in Refs. [28,29]). In summary, quasiparticle excitation energies were computed as a first-order correction to DFT within the generalized gradient approximation of PBE, with starting DFT-PBE eigenvectors and eigenvalues taken from the SIESTA and QUANTUM ESPRESSO DFT package, which is compatible with the BERKELEYGW implementation. The frequency dependence of the dielectric function is obtained via the generalized plasmon-pole model and optical excitation energies by inclusion of electron-hole interaction from the solution of the Bethe-Salpeter equation (BSE) [27,30].

The supercell with lattice vector (z direction) was set to 40 Å to avoid interactions with periodic images and contains 99% of the charge density, and the Coulomb interaction cut-off radius was adjusted at distances larger than half of the unit cell size. The supercell dimensions are $12 \times 12 \times 40$ Å^3. The BSE sum was computed using 8 (16) valence × 8 (16) conduction states for MMOs. To build the dielectric function and self-energy, the total number of states is 2394 for monolayers, spanning an energy range greater than 35 eV above the highest occupied state. The dielectric function plane wave's cutoff is 160 eV.

Subsequent to our GW calculations, the BSE is solved within the Tamm-Dancoff and static approximations to compute the complex transverse dielectric function, $\epsilon(\omega) = \epsilon_1(\omega) + i\epsilon_2(\omega)$. The absorption coefficient $\alpha(\omega)$ is given by [31]

$$\alpha(\omega) = 2\omega\sqrt{1/2[-\epsilon_1(\omega) + \sqrt{\epsilon_1(\omega)^2 + \epsilon_2(\omega)^2}]}, \quad (1)$$

where ω has units of energy (in atomic units).

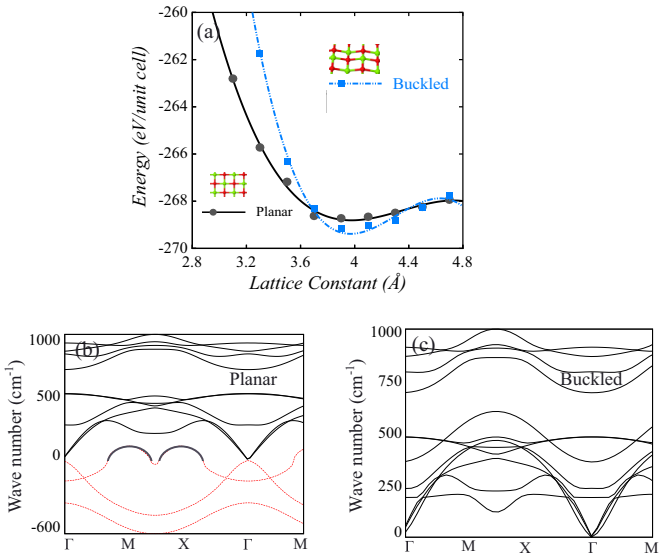

FIG. 1. The variation of energy with lattice constant of monolayer MgO(100) calculated by using LDA, for (a) the planar and the buckled structures. Phonon dispersion spectra of the planar (b) and the buckled (c) structures. The red-dashed lines indicate the imaginary frequency region for planar MgO(100).

III. BUCKLED STRUCTURE

In this section we perform DFT calculations for determining the lattice structure of MMOs. Each studied monolayer (2D-XO) consists of a (100) plane of MMO crystals where X = Mg, Ca, Mn, and Ni. We used a unit cell with 16 atoms and applied periodic boundary conditions. We found that the optimized buckled structure has lower energy than a planar 2D-XO(100). The buckled structure refers to the nonplanar lattices where, e.g., a Mg (Ca, Ni, and Mn) atom in the MgO lattice is in a different plane than the O atoms ($z_{\mathrm{Mg}} = +0.3$) and an even different plane than nearest Mg atoms $z_{\mathrm{Mg}} = -0.3$.

The variation of the total energy with lattice constant for planar and buckled MgO(100) is shown in Fig. 1(a). For 2D-MgO(100) (buckled structure) the lattice constant is found to be 3.9 Å, which is close to the lattice constant of bulk MgO [32] (4.191 Å) and is 1.3% larger than the lattice constant of MgO nanosheets [33] (3.85 Å). The out-of-plane height in the buckled structure is ±0.3 Å for Mg atoms and 0 Å for O atoms, which is in agreement with the results reported for MgO nanosheets [33]. For other MMOs the buckling heights and lattice constants are listed in Table I. The exceptional case is MnO, where we found that O atoms also move down and up, which is similar to the armchair configuration of fluorinated or hydrogenated graphene [34]. The structural deformation in the, e.g., Mg-O bonds (the buckling effect) is due to minimizing the repulsion between the $2p$ orbital of the O atom and the $3p$,$3d$ orbitals of the Mg atom. This improves the overlap between these orbitals.

In order to show that the buckled 2D-XO(100) is a stable 2D material, we performed phonon band-structure calculations. A typical phonon band structure at high-symmetry points for both planar and buckled structures of 2D-MgO(100) is shown in Figs. 1(b) and 1(c). There are 12 phonon branches including three acoustic branches with zero frequency at the zone center, and nine optical branches. It is seen that for the planar 2D-MgO(100) one acoustic and two optical phonon bands have imaginary frequencies. However, in the buckled structure [Fig. 1(c)] all the phonon modes have positive frequencies, which confirms the buckled structure is stable. It is interesting to note that the phonon dispersion frequency for the buckled structure is similar to that of bulk MgO [35–37].

We also performed finite temperature *ab initio* molecular dynamics (MD) simulations for buckled structures with the same unit cell (36 atoms) and found that this structure is thermodynamically stable at room temperature during a long-time MD simulation (1 ns). Therefore, hereafter our results are presented for the buckled 2D-XO's.

Notice the (optical and acoustic) phonon bands here are different than those for other 2D materials, e.g., graphene. The phonon frequencies (900 cm^{-1}) of MgO are lower than the optical frequency in graphene (1600 cm^{-1}) [26] as a result of the ionic bond between Mg and O atoms. However, the results are similar to the phonon spectrum of chlorographene, where the phonon spectrum is softened (1061 cm^{-1}) due to the saturation of C atoms with heavy Cl atoms. This is unlike that of the C-H bond in graphane and C-F in fluorinated graphene [38–40].

IV. ELECTRONIC STRUCTURE

A. MgO

In Figs. 2(a)–2(d) we compare the electronic band structure and corresponding density of states (DOS) and projected density of states (PDOS) of the buckled 2D-MgO(100) and bulk MgO acquired by the DFT-PBE results. As a first remark, both have direct band gaps and the Fermi energy of the bulk is lower than that of the buckled 2D structure. The valence bands (VBs) for both structures have less variation in the k space demonstrating the localized electronic states [41]. The lowest conduction band (CB) exhibits significant curvature in the k space. The upper conduction bands are flatter for the buckled 2D-MgO(100) as compared to the bulk MgO. The band-gap energy is estimated to be 3.82 eV (6.1 eV) for the 2D-MgO(100) (bulk MgO). The band gap for the buckled structure is comparable with that reported by Zhang *et al.*, i.e., 4.23 eV [33] for MgO nanosheets. The twofold degeneracy at the top of the CB in the bulk MgO is removed in the 2D-MgO(100) as compared to bulk MgO which is due to the broken symmetry in the low-dimensional system.

B. CaO

The electronic band structure of CaO and the corresponding DOS and PDOS are shown in Figs. 3(a)–3(c) acquired by DFT-PBE results. In Fig. 3(d) we depict the side and top views of the buckled 2D-CaO(100). We found that the 2D-CaO(100) have a direct band gap of 2.03 eV while bulk CaO, with the cubic rocksalt structure, exhibits insulator behavior with a wide band gap of 7.7 eV [42,43]. This is consistent with the experimentally observed decrease in the band gap of CaO thin film [44,45], i.e., Cui *et al.* have found the band gap of CaO thin film grown on Mo(100) to be 7.1 eV using a low-temperature scanning tunneling microscopy technique [44]. Notice that here our finding (2.03 eV) is for a monolayer

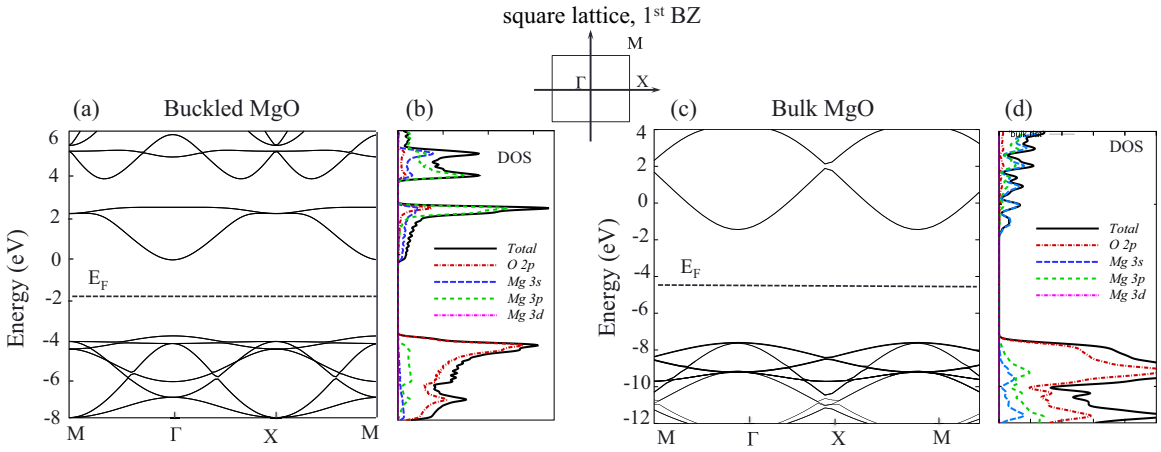

FIG. 2. The electronic band structure of spin up, total DOS, and PDOS of [(a),(b)] the buckled monolayer MgO(100) and [(c),(d)] bulk MgO, as obtained from DFT-PBE.

of CaO which is much thinner than the thin films studied in Refs. [44,45]. Therefore, because of a small, indirect band gap one can conclude that a monolayer of CaO(100) can show semiconducting properties.

Figures 2(b), 2(d), and 3(c) show that the CB is significantly a combination of cationic Mg (Ca) $3s$, $3p$, and $3d$ states, while the VB is drastically dominated by anionic O $2p$ states, as expected for an ionic oxide.

V. MnO AND NiO

The buckled 2D-MnO(100) and 2D-NiO(100) are found to have indirect band gaps which are about 0.88 and 1.21 eV, respectively. The latter is in contrast to the well-known direct band gap of bulk MnO and NiO [46–48]. In Figs. 4 and 5 the electronic band structure of the buckled 2D-MnO(100) and 2D-NiO(100) (for spin-up electrons), PDOS, and corresponding DOS diagrams for both spin-up and spin-down electrons are shown, acquired by DFT-PBE results. In Figs. 4(c) and 5(c), the PDOS reveals that VB is dominated by $3d$ states of cationic Mn and Ni. The electronic states for the spin up and spin down are different resulting in magnetic moments of $5\mu_B$ and $2\mu_B$ for 2D-MnO(100) and 2D-NiO(100), respectively. The top and side views of the buckled structure of the 2D-MnO(100) and 2D-NiO(100) are depicted in Figs. 4(d) and 5(d), respectively.

As already mentioned, the out-of-plane atoms in the buckled structure of 2D-MnO(100) are different than the others, i.e., some Mn atoms are in the same plane as O atoms.

In fact, antiferromagnetic properties occur among the 3D-bulk of transition-metal compounds, especially oxides such as NiO and MnO, i.e., the Mn^{2+} and Ni^{2+} ions are in one (111) plane and have a parallel spin alignment with each other and the ions in an adjacent (111) plane have antiparallel spin alignment. For bulk MnO and NiO, we found zero magnetic moment (AFM) while for 2D-MnO(100) and 2D-NiO(100) the magnetic moment is found to be $\sim 5\mu_B$ and $\sim 2\mu_B$ per unit cell [indicating ferromagnetic (FM) state], respectively.

The comparison of the total density of states of 2D-MnO(100) and 2D-NiO(100) for different values of U with the LDA+U approach is shown in Figs. 6(a)–6(h). These figures manifest that the LDA+U band gaps in MnO and NiO increase nonlinearly with increasing U, as changes in the p-d hybridization. Our results are in line with the U dependence of monoxide band gaps reported in the previous works [47,49].

Yamijala, *et al.* [50] reported that graphene quantum dots with edges doped with boron nitride show spin dependency of the highest occupied molecular orbital and the lowest unoccupied molecular orbital gap, because of the intrinsic electric field (charge transfer between B and N) present in the system [50]. They proposed, if the spin degeneracy at the zigzag edge

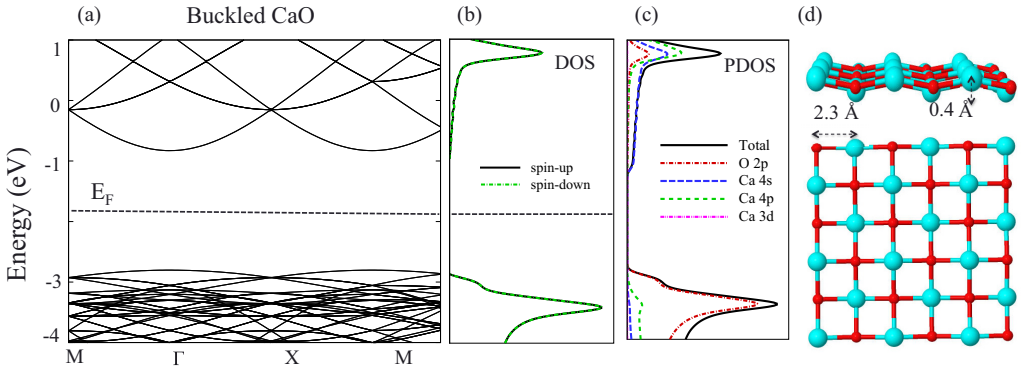

FIG. 3. (a) The electronic band structure of spin up, (b) total DOS, and (c) PDOS of the buckled monolayer CaO(100). (d) The side and top views of the buckled structure of monolayer CaO(100), from DFT-PBE.

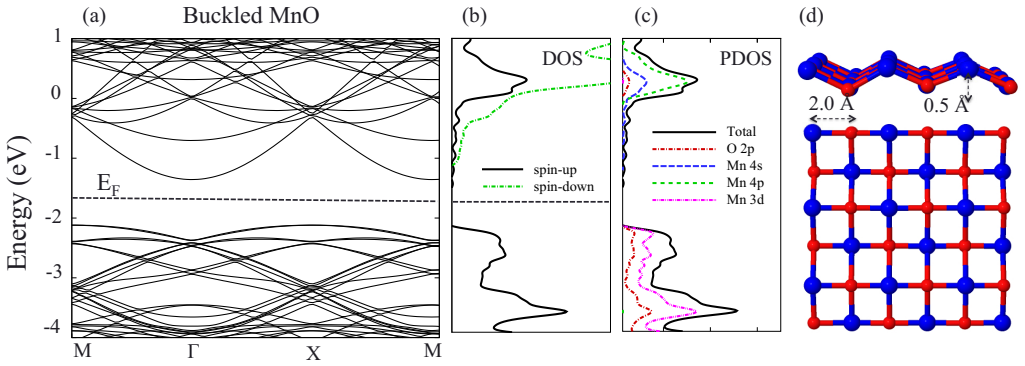

FIG. 4. (a) The electronic band structure of spin up, (b) total DOS, and (c) PDOS of the buckled monolayer MnO(100). (d) The side and top views of the buckled structure of monolayer MnO(100), from DFT-PBE.

can be broken by using methods such as doping [51], external electric field [52], strain [53], and substitution [50,54], the system will create magnetic moments. To discover the origin of the magnetic moment of 2D-MnO(100) and 2D-NiO(100), a simulated scanning tunneling microscopy (STM) image was obtained for 2D-MnO(100) and 2D-NiO(100) using a numerical STM tool for probing the electronic states and state mixing. Figure 7 gives two perspectives of the topographic simulated STM images calculated above the structures. Computing a STM image of MnO and NiO reveals subtle information on the variation of their electronic properties and the extra electronic states, with green protrusions related to negative charge accumulation on MnO and NiO consistent with broken local symmetry (local spin rotation) due to the computed DFT electrical dipole moment (intrinsic electric field) of 0.13 D for 2D-MnO(100) and 0.076 D for 2D-NiO(100). The magnetic superexchange interaction in manganites depends on the MnOMn bond angle [55,56]. Orbitally degenerate structures will undergo a geometry and electronic states distortion that lifts the degeneracy [56]. The main physical reason for the appearance of the FM state in monolayer MnO and NiO is as follows. For bulk MnO (and NiO), because Mn^{+2} (Ni^{+2}) is connected at 180° to the bridging nonmagnetic O^{-2}, there is a coupling between two next-to-nearest neighbor Mn^{+2} (Ni^{+2}) through O^{-2} resulting in an antiferromagnetic coupling. However, when the cation-anion-cation bond angle deviates from 180° the interaction can be ferromagnetic where the direct and indirect exchange mechanisms compete with each other. The 2D-MnO and NiO are found to be nonplanar in our calculations corresponding to the latter situation and therefore we do not expect an antiferromagnetic state. This symmetry breaking at the plane of (100) of monolayer monoxides induces a surface ferromagnetic layer, consistent with previous reports [57]. Moreover, we computed the Mulliken charge distribution to figure out the ferromagnetic origin of 2D-MnO and NiO monolayers. Figures 8(a) and 8(b) show the corresponding Mulliken charge distribution obtained by using the spin polarized calculations. The black and gray bars show the charge of spin up and spin down, respectively (for the Mn and Ni atoms). The empty and the filled blue bars indicate the charge of spin up and spin down, respectively (for the O atoms), which are almost equal. It can be seen that the charge difference between the spin up and spin down of the Mn and Ni atoms is $5\mu_B$ and $2\mu_B$, respectively. On the other hand, due to p-d hybridization the O-p states are admixed in the nominally d band. The latter implies a larger O-p moment for MnO than for NiO simply because the spin polarization in MnO is larger.

The splitting of the PDOS of the Mn and Ni atoms is shown in Figs. 8(c) and 8(d). The solid and dashed lines refer to the PDOS of the spin up and the spin down, which have different energy and PDOS. The different magnetic moments of 2D-MnO(100) and 2D-NiO(100) are related to the number of unpaired electrons in their d orbitals.

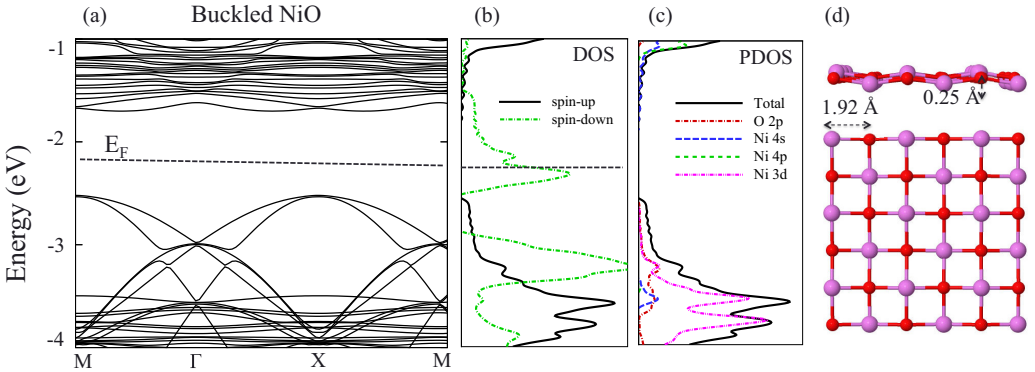

FIG. 5. (a) The electronic band structure of spin up, (b) total DOS, and (c) PDOS of the buckled monolayer NiO(100). (d) The side and top views of the buckled structure of monolayer NiO(100), from DFT-PBE.

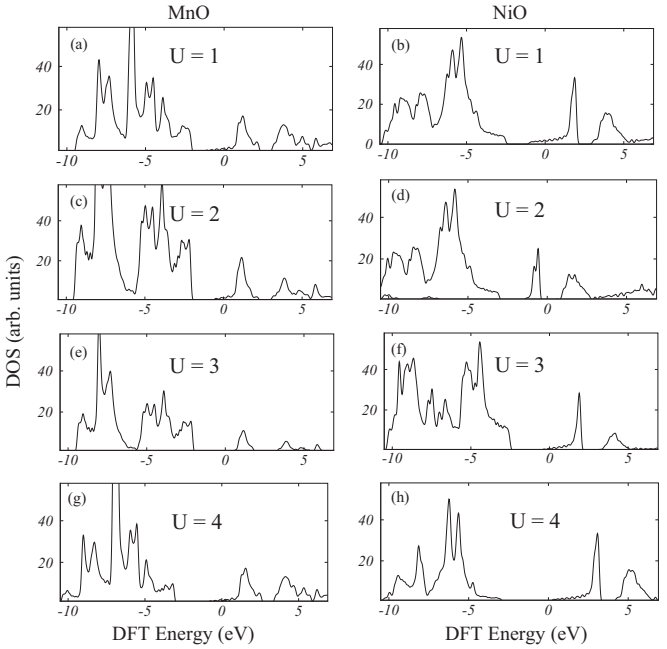

FIG. 6. Comparison of the total density of states of monolayer MnO(100) [(a),(c),(e),(g)] and monolayer NiO(100) [(b),(d),(f),(h)] for different values of U_{eff} obtained with the LDA+U approach.

Optical properties

Single-photon quantum emission from two-dimensional materials at room temperature has been studied by Tran and his collaborators which reveals an unprecedented potential for nanophotonics and quantum information processing [58]. They simulated the optical response of defects in two-dimensional sheets by using density functional theory and by calculating the imaginary dielectric tensor [58]. Meanwhile, for the solar cell applications, a photocatalytic material should have a wide absorption range of the solar and visible energy, e.g., 1.5–3.5 eV and a band gap between 2 and 3 eV [59]. The electronic band structures of 2D-MgO(100) and bulk MgO are shown in Figs. 2(a) and 2(c). It was found that the monolayer MgO has a smaller direct band gap than bulk MgO.

The optical absorption spectrum was obtained by calculating the real and imaginary parts of the complex dielectric function ($\epsilon = \epsilon_1 + i\epsilon_2$) using Eq. (1). In Figs. 9(a)–9(d) we compare the optical absorption spectrum of 2D-MgO(100) and bulk MgO. The solid lines (dashed lines) refer to the excitation: interacting electron-hole (noninteracting electron-hole). For the buckled 2D-MgO(100) we obtain the first peak at 1.58 eV and the second peak at 3.87 eV, which are very close to the visible light range (i.e., 1.64–3.2 eV) [see Fig. 9(a)] [59]. The optical absorption spectrum indicates a blue-shift light absorption range for MgO bulk due to its larger electronic band gap.

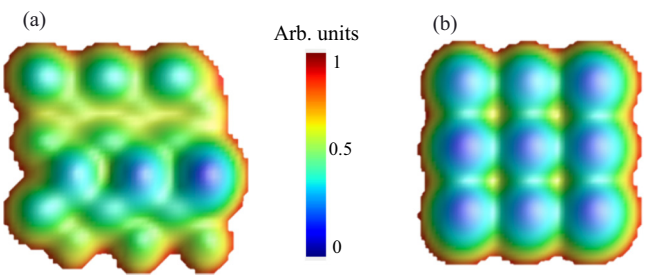

FIG. 7. Simulated STM images from top, for MnO(100) (a) and for NiO(100) (b). STM images were calculated with $I = 0.1$ nA and $V_b = -0.5$ V.

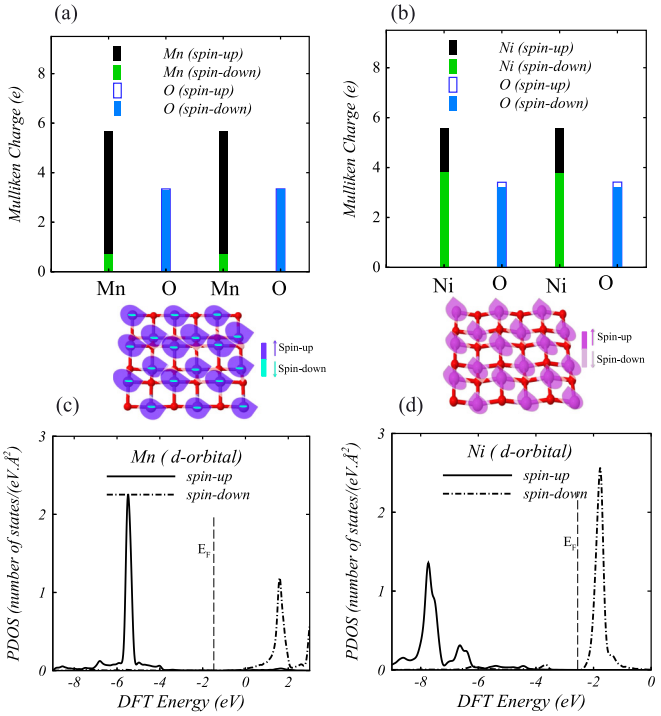

FIG. 8. Mulliken charge distribution for (a) Mn, O and (b) Ni, O atoms. Black and gray bars indicate the charge of spin up and spin down of Mn and Ni atoms, and the empty and filled blue bars indicate the charge of spin up and spin down of the O atoms. The spatial spin-density distribution for Mn and Ni ($\rho\uparrow - \rho\downarrow$) is also plotted (Mn: spin up, blue; spin down, green; Ni: spin up, violet; spin down, pink) (c), (d) Splitting of PDOS of 3d orbital for spin up and spin down of MnO(100) and NiO(100).

The absorption spectrum of the 2D-CaO(100), 2D-MnO(100), and 2D-NiO(100) are shown in Figs. 9(e)–9(p). Despite the small direct band gap of 2D-CaO(100), it has no absorption peak in visible light range. An absorption occurs at 2.5 eV for 2D-MnO(100) which is relevant to the results reported by Pandey *et al.* [60], where they have reported optical properties of synthesized MnO nanoparticles (colloidal solution) using UV-visible absorption spectroscopy. The absorption spectrum of 2D-NiO(100) contains several peaks in the range 1.5–3 eV, which are perfectly in the visible light range. This is in agreement with the absorption spectrum of NiO nanoparticles found by Hosny [61] and Jiang *et al.* [62], where several peaks in the visible light range have been reported. The GW gaps for the 2D-MnO(100) and 2D-NiO are found to be 1.7 and 1.9 eV, respectively, which are promising

We estimate the GW gap using GW calculations [see Figs. 9(b) and 9(d)]. The GW gap for the 2D-MgO(100) (bulk) is found to be ∼3.3 eV (∼9 eV).

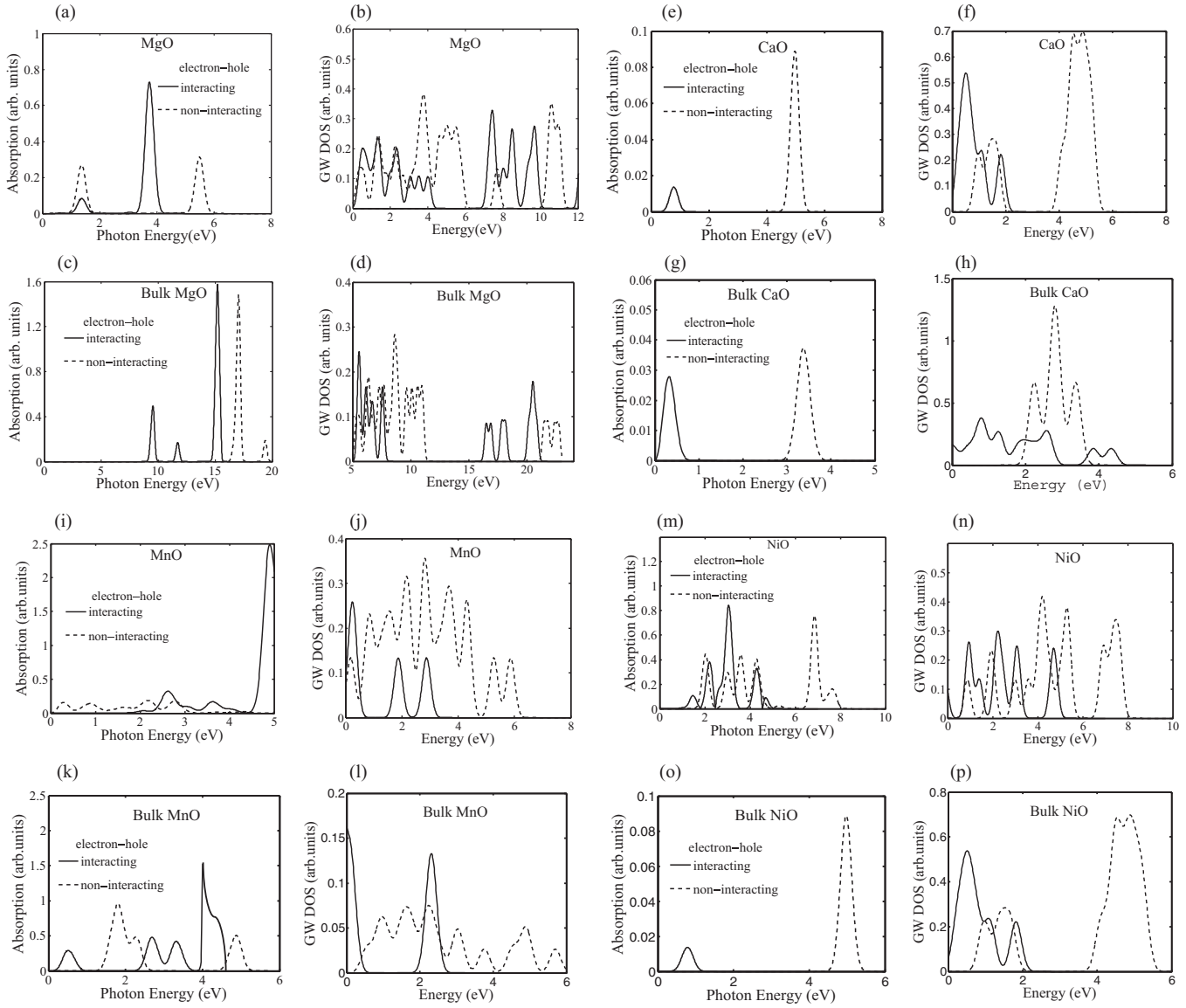

FIG. 9. (a) Comparison of the optical absorption spectrum computed for the $XO(100)$ monolayers (X = Mg, Ca, Mn, and Ni) and their bulk in two different phases; for interacting (solid line) and for noninteracting electron-hole case (dashed line), i.e., (a) and (b) are the results for monolayer MgO(100) and (b) and (c) are for bulk MgO, etc.

for photovoltaic applications (Table II). Jiang *et al.* studied the optical properties of crystalline NiO films, prepared by electron-beam deposition on quartz substrate [62], and found a strong ultraviolet emission at 377 nm for cubic structure along the (111) plane. As seen in Fig. 9(o), the absorption spectrum for bulk NiO has peaks in the infrared and ultraviolet range.

TABLE II. Comparison of the energy gap of monolayer MnO(100) and monolayer NiO(100) with the GW gap for different values of U with the LDA+U and GGA+U approaches.

Energy gap	MnO		NiO	
(eV)	(LDA+U	GGA+U)	(LDA+U	GGA+U)
$U = 1$	0.88	1.18	1.21	1.45
$U = 2$	1.33	1.56	2.04	2.31
$U = 3$	1.95	2.18	2.67	2.83
$U = 4$	2.37	2.65	2.96	3.34
GW gap	2.03		2.57	

VI. ELASTIC PROPERTIES

Here we investigate the mechanical properties of 2D-$XO(100)$. The elastic properties of these structures can be conveniently characterized by their linear response to an external in-plane stress, i.e., estimating the in-plane stiffness "C," which is equivalent to 2D-Young's modulus. Using S as the equilibrium area of the unit cell of a typical 2D-$XO(100)$ structure, the in-plane stiffness is obtained as $C = \frac{\frac{\delta^2 E_T}{\delta^2 \epsilon}}{S}$, where E_T is the total energy and ϵ is the uniaxial strain. Calculating the variation of the total energy with respect to the applied

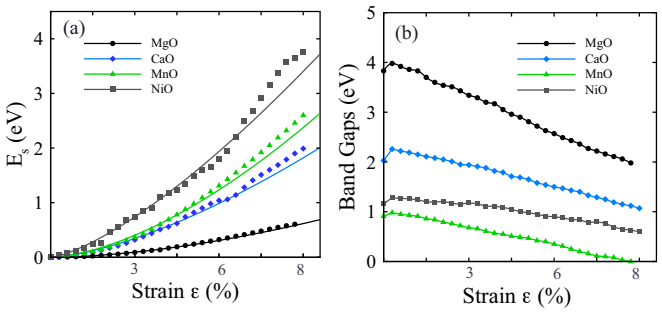

FIG. 10. The variation of the total energy (a) and electronic band gap with applied strain (b).

in-plane strain gives the in-plane stiffness [see Fig. 10(a)]. The in-plane stiffness for four 2D-XO(100)'s are listed in Table I. We also found a linear decrease in the electronic band gap with respect to the applied strain [Fig. 10(b)]. The largest (smallest) in-plane stiffness is found for 2D-NiO(100) [2D-MgO(100)]. The energy gap variation with strain is also maximum for NiO(100).

VII. DISCUSSION AND CONCLUSIONS

Reducing size can change the magnetic and optoelectronic properties of the thin films of MMOs which are considerably different from those of bulk. The so-called Mermin-Wagner theorem states that the systems with short-range interactions in one or two dimensions, because of intrinsic thermal fluctuations, cannot develop long-range magnetic order at finite temperature [63]. The Mermin-Wagner theorem is invoked to explain the absence of long-range order at finite temperatures. Strictly speaking, this would mean, however, that the Néel temperature is zero. There has been a long discussion about the importance of the Mermin-Wagner theorem for long-range order in 2D materials (rippling of graphene), and it has been concluded that the Mermin-Wagner theorem is not important at relevant length scales [64]. We found magnetic order, but a low transition temperature is expected to be strongly reduced to low dimension of the studied system [65,66]. We showed that the (100) lattice structure of MgO, CaO, MnO, and NiO is stable and is not flat. We found that the stable structure of the metallic monoxides is a buckled structure with a buckling height less than 1 Å and with different electronic and optical properties than those of their bulk.

In the bulk of transition-metal oxides (MnO and NiO), as already mentioned, cations are located in the (111) planes. The latter creates two opposing magnetic moment sublattices and consequently zero total magnetic moment. The cations in different sublattices are connected by 90° oxygen bonds resulting in the AFM order. The 2D allotropes of MnO and NiO in the (100) are found to have magnetic moments of $5\mu_B$ and $2\mu_B$, respectively, as a consequence of the broken symmetry of local electronic density of states. On the other hand, since bulk NiO and bulk MgO have the same lattice structure with infinitesimal lattice mismatch (0.2%), the high-quality NiO thin films (25 ML) can be grown on MgO(100) crystal [67]. MnO and NiO can also be deposited on Ag(100) single crystal and exhibit the thickness-dependent AFM anisotropy [20,68]. By using *ab initio* calculations, we found the lattice mismatch between 2D-NiO(100) and 2D-MgO(100) is even smaller (0.15%), which is promising for the synthesis of NiO-MgO bilayer and multilayer.

Furthermore, it is well known that a semiconductor with a band gap between 1.0 and 1.5 eV, or near-infrared light, have the highest efficiency for potential applications in solar cells. The solar cells made of thin-film technologies have not yet been commercially developed and they are still in the research phase. Here we found that the GW gap (GW/BSE) is about 2.05 and 2.57 eV for the 2D-MnO(100) and 2D-NiO(100), respectively. There are several peaks in the absorption spectrum of the 2D-NiO(100) which are located at the visible light region. The latter is promising for fabricating new thin-film-based photovoltaic solar cells. In summary, these findings of monolayer of metallic monoxides have important applications in thin-film technologies, nanoelectronics, spintronics, and solar cells using 2D materials with tunable opto-electro-thermo-mechanical properties using different number of layers.

Finally, we discuss whether or not these monolayer crystals can be stable in nature. Indeed the synthesis of isolated MMOs is difficult, however, MMO deposition over inert substrates or encapsulating them by graphene or other 2D material membranes can be realized. Recently, we proposed that by using a graphene bilayer as a scaffold, the synthesis of silicene with electronic properties decoupled from the substrate would be possible [69]. The recent observation of the conversion of a graphene encapsulated aqueous salt solution to 2D crystals [6] of a corresponding metal oxide is an encouraging route to follow.

ACKNOWLEDGMENTS

This work was supported by the Flemish Science Foundation (FWO-Vl) and the Methusalem program. M.N.-A. was supported by Iran National Science Foundation (INSF).

[1] K. S. Novoselov, A. K. Geim, S. V. Morozov, D. Jiang, Y. Zhang, S. V. Dubonos, I. V. Grigorieva, and A. A. Firsov, Science **306**, 666 (2004).

[2] A. K. Geim and I. V. Grigorieva, Nature (London) **499**, 419 (2013).

[3] C. Ataca, H. Sahin, and S. Ciraci, J. Phys. Chem. C **116**, 8983 (2012).

[4] H. Duan, N. Yan, R. Yu, C.-R. Chang, G. Zhou, H.-S. Hu, H. Rong, H. Niu, J. Mao, H. Asakura, T. Tanaka, P. J. Dyson, J. Li, and Y. Li, Nat. Commun. **5**, 3093 (2014).

[5] X. Yin, X. Liu, Y.-T. Pan, K. A. Walsh, and H. Yang, Nano Lett. **14**, 7188 (2014).

[6] K. S. Vasu, E. Prestat, J. Abraham, J. Dix, R. J. Kashtiban, J. Beheshtian, J. Sloan, P. Carbone, M. Neek-Amal, S. J. Haigh, A. K. Geim, and R. R. Nair, Nat. Commun. **7**, 12168 (2016).

[7] L. Ben-Dor, R. Druilhe, and P. Gibart, J. Cryst. Growth **24–25**, 172 (1974).

[8] A. Malashevich, E. I. Altman, and S. Ismail-Beigi, Phys. Rev. B **90**, 165426 (2014).

[9] H.-J. Freund, H. Kuhlenbeck, and V. Staemmler, Rep. Prog. Phys. **59**, 283 (1996).

[10] M. D. Irwin, D. B. Buchholz, A. W. Hains, R. P. H. Chang, and T. J. Marks, Proc. Natl. Acad. Sci. U.S.A. **105**, 2783 (2008).

[11] C. Giovanardi, A. di Bona, T. S. Moia, S. Valeri, C. Pisani, M. Sgroi, and M. Busso, Surf. Sci. **505**, L209 (2002).

[12] X. Shao, P. Myrach, N. Nilius, and H.-J. Freund, J. Phys. Chem. C **115**, 8784 (2011).

[13] M. D. Towler, N. L. Allan, N. M. Harrison, V. R. Saunders, W. C. Mackrodt, and E. Apra, Phys. Rev. B **50**, 5041 (1994).

[14] L. Néel, Rev. Mod. Phys. **25**, 58 (1953).

[15] P. W. Anderson, Phys. Rev. **79**, 350 (1950).

[16] Lamberto Duò, Marco Finazzi, and Franco Ciccacci, *Magnetic Properties of Antiferromagnetic Oxide Materials* (Wiley-VCH, Weinheim, 2010).

[17] S.-W. Cheong, Nat. Mater. **6**, 927 (2007).

[18] P. Grünberg, R. Schreiber, Y. Pang, M. B. Brodsky, and H. Sowers, Phys. Rev. Lett. **57**, 2442 (1986).

[19] M. N. Baibich, J. M. Broto, A. Fert, F. Nguyen Van Dau, F. Petroff, P. Etienne, G. Creuzet, A. Friederich, and J. Chazelas, Phys. Rev. Lett. **61**, 2472 (1988).

[20] F. Muller, R. de Masi, D. Reinicke, P. Steiner, S. Hufner, and K. Stowe, Surf. Sci. **520**, 158 (2002).

[21] F. Allegretti, C. Franchini, V. Bayer, M. Leitner, G. Parteder, B. Xu, A. Fleming, M. G. Ramsey, R. Podloucky, S. Surnev, and F. P. Netzer, Phys. Rev. B **75**, 224120 (2007).

[22] P. S. Patil and L. D. Kadam, Appl. Surf. Sci. **199**, 211 (2002).

[23] S. Sriram and A. Thayumanavan, Int. J. Mater. Sci. Eng. **1**, 118 (2013).

[24] C.-H. Ho, Y.-M. Kuo, C.-H. Chan, and Y.-R. Ma, Sci. Rep. **5**, 15856 (2015).

[25] J. M. Soler, E. Artacho, J. D. Gale, A. García, J. Junquera, P. Ordejón, and D. J. Sánchez-Portal, J. Phys.: Condens. Matter **14**, 2745 (2002).

[26] B. B. Karki and R. M. Wentzcovitc, Phys. Rev. B **61**, 8793 (2000).

[27] J. Deslippe, G. Samsonidze, D. A. Strubbe, M. Jain, M. L. Cohen, and S. G. Louie, Comput. Phys. Commun. **183**, 1269 (2012).

[28] S. Sharifzadeh, A. Biller, L. Kronik, and J. B. Neaton, Phys. Rev. B **85**, 125307 (2012).

[29] S. Sharifzadeh, P. Darancet, L. Kronik, and J. B. Neaton, J. Phys. Chem. Lett. **4**, 2197 (2013).

[30] M. S. Hybertsen and S. G. Louie, Phys. Rev. B **34**, 5390 (1986).

[31] G. Grosso and G. Parravicini, *Solid State Physics*, 2nd ed. (Academic, London, 2014).

[32] R. Coquet, G. J. Hutchings, S. H. Taylor, and D. J. Willock, J. Mater. Chem. **16**, 1978 (2006).

[33] Y. G. Zhang, H. Y. He, and B. C. Pan, J. Phys. Chem. C **116**, 23130 (2012).

[34] S. K. Singh, S. G. Srinivasan, M. Neek-Amal, S. Costamagna, A. C. T. van Duin, and F. M. Peeters, Phys. Rev. B **87**, 104114 (2013).

[35] G. Peckham, Proc. Phys. Soc. **90**, 657 (1967).

[36] M. J. L. Sangster, G. Peckham, and D. H. Saunderson, J. Phys. C **3**, 1026 (1970).

[37] P. H. Dederichs, H. Schober, and D. J. Sellmyer, *Phonon States of Elements. Electron States and Fermi Surfaces of Alloys / Phononenzustände von Elementen. Elektronenzustände und Fermiflächen von Legierungen* (Springer-Verleg, Berlin, 1981).

[38] H. Peelaers, A. D. Hernandez-Nieves, O. Leenaerts, B. Partoens, and F. M. Peeters, Appl. Phys. Lett. **98**, 051914 (2011).

[39] H. Sahin, M. Topsakal, and S. Ciraci, Phys. Rev. B **83**, 115432 (2011).

[40] H. Sahin and S. Ciraci, J. Phys. Chem. C **116**, 24075 (2012).

[41] R. H. French, R. V. Kasowski, F. S. Ohuchi, D. J. Jones, H. Song, and R. L. Coble, J. Am. Ceram. Soc. **73**, 3195 (1990).

[42] M. A. Bolorizadeh, V. A. Sashin, A. S. Kheifets, and M. J. Ford, J. Electron. Spectrosc. **141**, 27 (2004).

[43] *Handbook of Laser and Science and Technology*, edited by M. J. Weber (CRC, Boca Raton, 1995), Supplement 2: Optical Materials.

[44] Y. Cui, S. Tosoni, W.-D. Schneider, G. Pacchioni, N. Nilius, and H.-J. Freund, Phys. Rev. Lett. **114**, 016804 (2015).

[45] S. Schintke, S. Messerli, M. Pivetta, F. Patthey, L. Libioulle, M. Stengel, A. De Vita, and W.-D. Schneider, Phys. Rev. Lett. **87**, 276801 (2001).

[46] A. Ghosh, C. M. Nelson, L. S. Abdallah, and S. Zollner, J. Vac. Sci. Technol. A **33**, 061203 (2015).

[47] H. Jiang, R. I. Gomez-Abal, P. Rinke, and M. Scheffler, Phys. Rev. B **82**, 045108 (2010).

[48] M. Vignesh Kumar, S. Muthulakshmi, A. Alfind Paulfrit, J. Pandiarajan, N. Jeyakumaran, and N. Prithivikumaran, Int. J. Chem. Tech. Res. **6**, 5174 (2014).

[49] M. Forti, P. Alonso, P. Gargano, and G. Rabiolo, Proc. Mater. Sci. **1**, 230 (2012).

[50] S. S. Yamijala, A. Bandyopadhyay, and S. K. Pati, J. Phys. Chem. C **117**, 23295 (2013).

[51] S. Dutta and S. K. Pati, J. Phys. Chem. B **112**, 1333 (2008).

[52] S. Dutta, A. K. Manna, and S. K. Pati, Phys. Rev. Lett. **102**, 096601 (2009).

[53] L. Kou, C. Tang, W. Guo, and C. Chen, ACS Nano **5**, 1012 (2011).

[54] B. Ershaad Ahamed, P. Prakash, and K. P. Swapan, New J. Phys. **13**, 053008 (2011).

[55] H. Y. Hwang, S.-W. Cheong, P. G. Radaelli, M. Marezio, and B. Batlogg, Phys. Rev. Lett. **75**, 914 (1995).

[56] P. Zubko, S. Gariglio, M. Gabay, P. Ghosez, and J.-M. Triscone, Annu. Rev. Condens. Matter Phys. **2**, 141 (2011).

[57] F. Pressacco, V. Uhl, M. Gatti, A. Bendounan, E. E. Fullerton, and F. Sirotti, Sci. Rep. **6**, 22383 (2016).

[58] T. T. Tran, K. Bray, M. J. Ford, M. Toth, and I. Aharonovich, Nat. Nanotechnol. **11**, 37 (2016).

[59] H. Zhang, C.-J. Tong, Y. Zhang, Y.-N. Zhang, and L.-M. Liu, J. Mater. Chem. A **3**, 9632 (2015).

[60] B. K. Pandey, A. K. Shahi, and R. Gopal, Appl. Surf. Sci. **283**, 430 (2013).

[61] N. M. Hosny, Polyhedron **30**, 470 (2011).

[62] D. Y. Jiang, J. M. Qin, X. Wang, S. Gao, Q. C. Liang, and J. X. Zhao, Vacuum **86**, 1083 (2012).

[63] N. D. Mermin and H. Wagner, Phys. Rev. Lett. **17**, 1133 (1966).

[64] R. C. Thompson-Flagg, M. J. B. Moura, and M. Marder, Europhys. Lett. **85**, 46002 (2009).

[65] E. N. Abarra, K. Takano, F. Hellman, and A. E. Berkowitz, Phys. Rev. Lett. **77**, 3451 (1996).

[66] D. Alders, L. H. Tjeng, F. C. Voogt, T. Hibma, G. A. Sawatzky, C. T. Chen, J. Vogel, M. Sacchi, and S. Iacobucci, Phys. Rev. B **57**, 11623 (1998).

[67] S. Altieri, M. Finazzi, H. H. Hsieh, M. W. Haverkort, H.-J. Lin, C. T. Chen, S. Frabboni, G. C. Gazzadi, A. Rota, S. Valeri, and L. H. Tjeng, Phys. Rev. B **79**, 174431 (2009).

[68] C. Giovanardi, A. di Bona, S. Altieri, P. Luches, M. Liberati, F. Rossi, and S. Valeri, Thin Solid Films **428**, 195 (2003).

[69] M. Neek-Amal, A. Sadeghi, G. R. Berdiyorov, and F. M. Peeters, Appl. Phys. Lett. **103**, 261904 (2014).

[70] R. M. Ribeiro and N. M. R. Peres, Phys. Rev. B **83**, 235312 (2011).

[71] K. Kobayashi and J. Yamauchi, Phys. Rev. B **51**, 17085 (1995).

[72] K. Liu, Q. Yan, M. Chen, W. Fan, Y. Sun, J. Suh, D. Fu, S. Lee, J. Zhou, S. Tongay, J. Ji, J. B. Neaton, and J. Wu, Nano Lett. **14**, 5097 (2014).

[73] O. Madelung, U. Russler, and M. Schulz, *Landolt-Burnstein-Group III Condensed Matter, II-VI and I-VII Compounds; Semimagnetic Compounds* (Springer-Verlag, Berlin, 1999), Vol. 41B.